

## Article

# Multi-Timescale Estimation of SOE and SOH for Lithium-Ion Batteries with a Fractional-Order Model and Multi-Innovation Filter Framework

Jing Yu  and Fang Yao \* 

State Key Laboratory of Reliability and Intelligence of Electrical Equipment, Hebei University of Technology, Tianjin 300401, China; 202321401143@stu.hebut.edu.cn

\* Correspondence: yaofang@hebut.edu.cn

## Abstract

Based on a fractional-order equivalent circuit model, this paper proposes a multi-timescale collaborative State of Energy (SOE) and State of Health (SOH) estimation method (FOASTFREKF-EKF) for lithium batteries to mitigate the influence of model inaccuracies and battery aging on SOE estimation. Initially, a fractional-order equivalent circuit model is built, and its parameters are identified offline using the Starfish Optimization Algorithm (SFOA) to establish a high-fidelity battery model. An  $H\infty$  filter is then integrated to improve the algorithm's resilience to external disturbances. Furthermore, an adaptive noise covariance adjustment mechanism is employed to reduce the effect of operational noise, and a time-varying attenuation factor is introduced to improve the algorithm's tracking and convergence capabilities during abrupt system-state changes. A joint estimator is subsequently constructed, which uses an Extended Kalman Filter (EKF) for the online determination of battery parameters and SOH assessment. This approach minimizes the effect of varying model parameters on SOE accuracy while reducing computational load through multi-timescale methods. Experimental validation under diverse operating conditions shows that the proposed algorithm achieves root mean square errors (RMSE) of less than 0.21% for SOE and 0.31% for SOH. These findings demonstrate that the method provides high accuracy and reliability under complex operating conditions.



Academic Editor: Xiaopeng Tang  
and Xin Lai

Received: 16 September 2025

Revised: 3 October 2025

Accepted: 6 October 2025

Published: 10 October 2025

**Citation:** Yu, J.; Yao, F. Multi-Timescale Estimation of SOE and SOH for Lithium-Ion Batteries with a Fractional-Order Model and Multi-Innovation Filter Framework. *Batteries* **2025**, *11*, 372. <https://doi.org/10.3390/batteries11100372>

**Copyright:** © 2025 by the authors. Licensee MDPI, Basel, Switzerland. This article is an open access article distributed under the terms and conditions of the Creative Commons Attribution (CC BY) license (<https://creativecommons.org/licenses/by/4.0/>).

**Keywords:** fractional-order model; adaptive mechanisms; strong tracking filter; SOE; SOH

## 1. Introduction

Driven by the global energy system's transformation towards clean and low-carbon, the popularity of electric vehicles (EVs) is increasing [1,2]. Lithium-ion batteries have become the primary power source for EVs due to their characteristics, including long cycle life, high energy density, and no memory effect [3,4]. However, the complex internal degradation mechanisms of these batteries are highly coupled, nonlinear, and time-varying, which complicates accurate state estimation. Accurately estimating the State of Energy (SOE) and State of Health (SOH) of batteries is crucial for a battery management system (BMS), as it directly influences operational safety, energy management efficiency, and lifetime prediction accuracy [5]. Consequently, high-precision, real-time joint estimation of SOE and SOH is critical for advancing battery management technology.

State of Energy (SOE) is a vital parameter that describes the dynamic charging and discharge process of lithium-ion batteries. It is defined as the ratio of a battery's remaining

energy to its rated energy. According to current research, battery SOE estimate techniques may be broadly divided into three categories: power integration methods, data-driven methods, and model-based methods [6–8]. The power integration method determines SOE by cumulatively integrating current over time, benefiting from computational simplicity. However, its reliance on an accurate initial SOE value and sensitivity to cumulative errors restrict its widespread application [9]. In contrast, data-driven methods utilize operational data (e.g., current, voltage) with machine learning algorithms to estimate SOE without an explicit battery model, thereby capturing complex nonlinear relationships. A key drawback, however, is their dependence on large training datasets and potentially limited robustness in unseen scenarios [10,11]. Consequently, model-based methods have garnered a lot of attention due to their simplicity, reliability, and stability. The model-based method achieves precise SOE estimation by fusing high-fidelity battery models with advanced filters, which dynamically correct the system state based on the difference between measured values and model predictions [12].

Based on battery models, the Kalman filter (KF) algorithm has become the mainstream technique for SOE estimation [13,14]. By minimizing the mean square error covariance of the state estimate, the Kalman filter (KF) provides the best unbiased estimation for linear Gaussian systems. It iteratively corrects predictions during operation and exhibits robust convergence even with initial state errors. However, the KF algorithm assumes that system noise statistics are stationary and follow a Gaussian distribution. In real-world battery systems, this assumption is often violated, which can lead to divergence or growing estimation errors due to noise mismatches. Consequently, researchers have developed several improved algorithms [15–18]. Due to its manageable computational complexity, the EKF has emerged as a common choice for nonlinear SOE estimation. Nevertheless, its performance is highly dependent on model accuracy and the empirical tuning of noise covariance matrices. This limitation necessitates the integration of adaptive mechanisms to ensure robustness across all operating conditions [19].

The accuracy of model-based methods is heavily reliant on how well the model represents the intricate electrochemical behavior of the battery. Therefore, establishing a precise battery model is essential [20]. Battery models are primarily categorized as electrochemical models and equivalent circuit models (ECMs). ECMs represent complex electrochemical systems using circuit-based networks. Despite utilizing only a limited number of electrical components, ECMs can achieve high accuracy and are divided into integer-order models (IOMs) or fractional-order models (FOMs) [21]. FOMs characterize battery dynamics more accurately than IOM, particularly for voltage transients under dynamic and non-equilibrium conditions. For instance, Reference [22] demonstrated that under diverse operating conditions, FOMs capture battery characteristics more accurately, significantly enhancing the precision of terminal voltage estimation. Given these advantages, FOMs are widely utilized for battery state estimation and performance optimization [23].

The accurate estimation of the State of Energy (SOE) is challenged by factors such as noise interference, state limitations, and parameter uncertainty during lithium-ion battery operation [24–26]. To address these challenges, several joint estimation methods have been proposed. For instance, Reference [27] presents a method that first updates battery model parameters and capacity in real-time before using UKF for joint SOE-SOH estimation. To mitigate SOE estimation errors caused by declining SOH, Reference [28] utilizes an enhanced dual extended Kalman filter (DEKF) algorithm to estimate SOE and SOH. However, many existing methods struggle with the highly complex nature of battery operation. Focusing on SOE estimation errors induced by environmental temperature and parameter coupling, Reference [25] proposes a collaborative estimation method of SOE and maximum available energy based on an adaptive dual-fractional-order Kalman filter, which

improves SOE accuracy by updating the maximum available energy in real time. However, existing methods often lack the responsiveness and adaptability to accommodate shifting operational conditions. Moreover, they frequently fail to systematically address the impact of time-varying noise on the stability and accuracy of filter estimates, which constrains their reliability in real-world applications. This challenge of achieving robust and accurate state estimation under uncertainty is a significant frontier in battery research. As a recent review of energy storage technologies has highlighted, there is growing recognition of the need to augment model-based estimators with adaptive mechanisms. Looking ahead, the integration of multi-physics sensor data will be essential for overcoming inherent limitations and enhancing reliability [29].

To address these gaps and meet the practical requirements of BMS, this study proposes a novel joint estimation approach for SOE and SOH based on a fractional-order adaptive strong-tracking robust EKF framework (FOASTFREKF-EKF).

The main contributions of this paper are as follows:

1. The algorithm incorporates adaptive theory and  $H\infty$  filtering to update noise statistics in real time, significantly enhancing the stability and accuracy of SOE estimation.
2. A time-varying attenuation factor is integrated into the filtering process to minimize dependence on historical data and improve sensitivity to sudden changes in operating conditions.
3. The framework explicitly accounts for the impact of battery aging on SOE. An EKF is employed for online battery parameter identification and SOH estimation, thereby improving the overall precision.
4. A multi-timescale strategy is adopted for the joint estimation of SOE and SOH to reduce computational complexity. The proposed method is validated using experimental data from a custom-built test platform. The results confirm its effectiveness and demonstrate its capabilities.

## 2. State Estimation of Lithium Batteries

The EKF is a prevalent technique for SOE estimation due to its effectiveness in dynamic state estimation. Although well-suited for high-dimensional nonlinear systems, the EKF algorithm suffers from reduced accuracy and robustness when applied to complex battery models. Furthermore, battery aging induces time-varying characteristics in the model parameters, causing batteries with identical SOE levels to exhibit markedly different behaviors depending on their varying degrees of degradation. Consequently, high-precision SOE estimation must account for the battery aging state as a critical influencing factor. To address these limitations, this section presents a novel FOASTFREKF-EKF algorithm. This method enhances the traditional EKF by integrating  $H\infty$  filtering and adaptive theory, and introduces a time-varying attenuation factor to lessen the model's reliance on historical data. The proposed framework explicitly incorporates the impact of battery aging and performs simultaneous online estimation of battery parameters, SOH, and SOE, thereby achieving significant improvements in both stability and accuracy.

### 2.1. Fractional-Order Model

Electrochemical impedance spectroscopy (EIS) characterizes the impedance changes of lithium-ion batteries at different frequencies [30]. The resulting data is commonly represented as a Nyquist plot, where the shape of specific regions corresponds to the changes in the internal state of the battery, as illustrated in Figure 1.

Traditional integer-order equivalent circuit models use ordinary differential equations to describe battery dynamics. These models' ideal capacitive elements neglect microscopic inhomogeneities at the electrode interface and thus fail to accurately fit the flattened

semicircle observed in the mid-frequency region of EIS, i.e., the “dispersion effect”. This results in significant discrepancies between the models and the experimental data. To better represent the nonlinear and dynamic electrochemical processes in lithium-ion batteries, this paper replaces the ideal capacitive components with a constant phase element (CPE). This modification enables the establishment of a fractional-order equivalent circuit model, as shown in Figure 2.

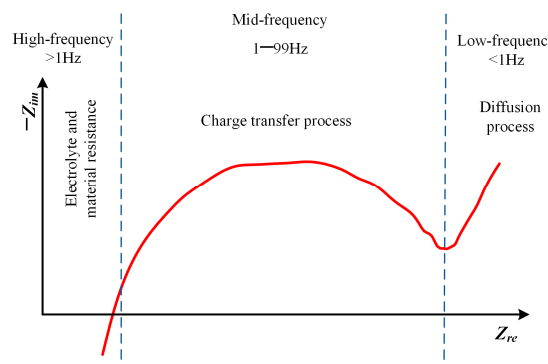


**Figure 1.** The impedance change curves at different frequencies.

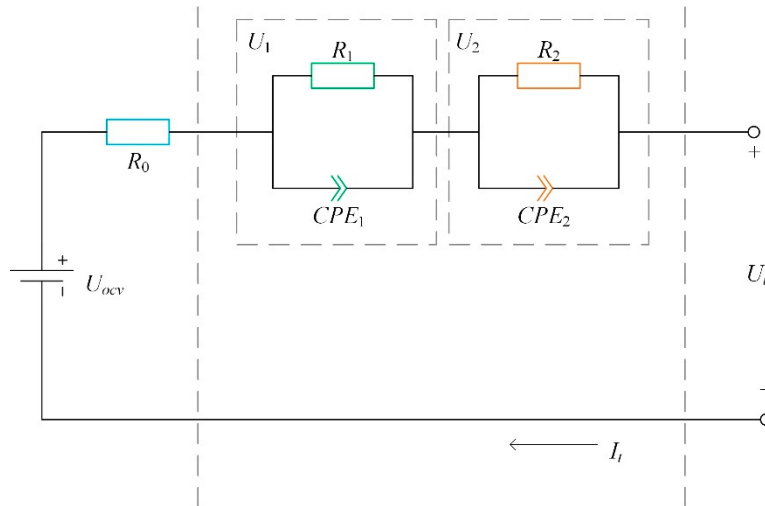


**Figure 2.** Fractional-order equivalent circuit model.

In this model,  $U_{ocv}$  is the open circuit voltage,  $R_0$  is the ohmic internal resistance,  $R_1$  and  $CPE_1$  are the polarization resistance and capacitance, respectively;  $R_2$  and  $CPE_2$  are the diffusion resistance and capacitance, respectively; and  $U_t$  is the terminal voltage. Based on Kirchhoff's laws of current and voltage, the state equations and observation equation for the fractional-order model are derived:

$$\left\{ \begin{array}{l} \frac{d^m U_1}{dt^m} = -\frac{1}{R_1 C_1} U_1 + \frac{1}{C_1} I_t \\ \frac{d^n U_2}{dt^n} = -\frac{1}{R_2 C_2} U_2 + \frac{1}{C_2} I_t \\ SOE(k+1) = SOE(k) - \frac{U_t(k) I_t(k) T_s}{E_n} \end{array} \right. \quad (1)$$

$$U_t = U_{OCV} - U_1 - U_2 - I_t R_0 \quad (2)$$

where  $U_1$  and  $U_2$  are the voltages across the resistance and capacitance,  $I_t$  is the operating current,  $m$  and  $n$  are respectively the orders of the  $CPE_1$  and  $CPE_2$ ,  $T_s$  is the time step, and  $E_n$  is the maximum available energy of the battery.

Equation (1) must be discretized for battery state estimation. The Grünwald-Letnikov (G-L) fractional calculus introduces the concept of discrete differences, which makes it

suitable for handling non-integer order calculus operations. Consequently, this paper processes fractional-order differential terms using the G-L fractional calculus. The definition of G-L fractional calculus is as follows:

$$D_t^a f(t) = \lim_{T_s \rightarrow 0} T_s^{-a} \sum_{j=0}^{[t/T_s]} (-1)^j \binom{a}{j} f(t - jT_s) \quad (3)$$

where  $D_t^a$  is the fractional order differential operator,  $a$  and  $t$  are the lower and upper limits of integration, respectively, and  $\binom{a}{j}$  is the binomial coefficient.

Equation (1) can be discretized as follows:

$$x_k = Ax_{k-1} + Bu_{k-1} - \sum_{j=1}^k K_j x_{k-j} \quad (4)$$

$$\text{where } x_k = \begin{bmatrix} U_{1,k} \\ U_{2,k} \\ SOE_k \end{bmatrix}, A = \begin{bmatrix} -\frac{T_s^m}{R_1 C_1} & 0 & 0 \\ 0 & -\frac{T_s^n}{R_2 C_2} & 0 \\ 0 & 0 & 1 \end{bmatrix}, B = \begin{bmatrix} \frac{T_s^m}{C_1} \\ \frac{T_s^n}{C_2} \\ -\frac{U_{t,k} T_s}{E_n} \end{bmatrix}, u_{k-1} = I_t(k-1),$$

$$K_j = \begin{bmatrix} (-1)^j \binom{m}{j} & 0 & 0 \\ 0 & (-1)^j \binom{n}{j} & 0 \\ 0 & 0 & 0 \end{bmatrix}.$$

Equation (2) simplifies to the following at time k after discretization:

$$y_k = Cx_k - R_0 u_k + U_{OCV} \quad (5)$$

$$\text{where } C_k = \begin{bmatrix} -1 & -1 & 0 \end{bmatrix}, y_k = U_t(k).$$

## 2.2. Parameter Identification

Based on the fractional-order equivalent circuit model established here, the following parameters now require identification:  $R_0$ ,  $R_1$ ,  $R_2$ ,  $CPE_1$ ,  $CPE_2$ ,  $m$ , and  $n$ . Fractional-order models usually use offline identification to guarantee identification accuracy and minimize computing complexity. To achieve optimal identification performance, this paper utilizes the Starfish Optimization Algorithm (SFOA), which has greater effectiveness than the mainstream Adaptive Genetic Algorithm (AGA) [31–33] for multi-parameter optimization. The SFOA effectively addresses AGA's limitations toward premature convergence and parameter sensitivity through its unique balanced search mechanism, which strategically integrates global exploration with local exploitation.

A recent heuristic algorithm called the Starfish Optimization Algorithm (SFOA) addresses optimization problems by emulating the collective behaviors of starfish, such as collaborative exploration, predation, and regeneration [34]. Exploration and exploitation are the two main phases of the SFOA. The exploration resembles the exploratory behavior of starfish. Depending on the dimensionality (D) of the optimization problem, the algorithm uses either a five-dimensional or one-dimensional search model for different optimization tasks. The exploitation phase simulates starfish predation and regeneration behaviors to update the population and converge toward the global optimum. Since starfish move slowly during regeneration, the regeneration phase of the SFOA is applied only to the last individual in the population ( $i = N$ ).

The key advantage of the SFOA is its effective balance between global exploration and local exploitation, enabled by a unique collaborative branch exploration mechanism and an adaptive regenerative process. These features collectively ensure the algorithm's efficient convergence and overall robustness.

The SFOA consists of the following steps:

- (1) Initialization: An initial population of starfish individuals is generated randomly, each representing a potential solution.
- (2) Calculate individual fitness: A fitness function is defined, and the fitness values for each starfish are computed at the current iteration.
- (3) Update starfish positions: In the exploration phase, the positions are updated according to the problem's dimensionality ( $D$ ). In the exploitation phase, positions are updated by simulating predation and regeneration.
- (4) Archive updates: The optimal positions of each starfish are updated by comparing its current fitness value with those of all other starfish.
- (5) Output results: When the iteration termination criteria are met, the SFOA ends, achieving identification of circuit model parameters.

Figure 3 illustrates the algorithm's flowchart, where  $\text{rand}$  denotes a random number within  $[0, 1]$ , and  $G_p$  is set to 0.5 in this study.

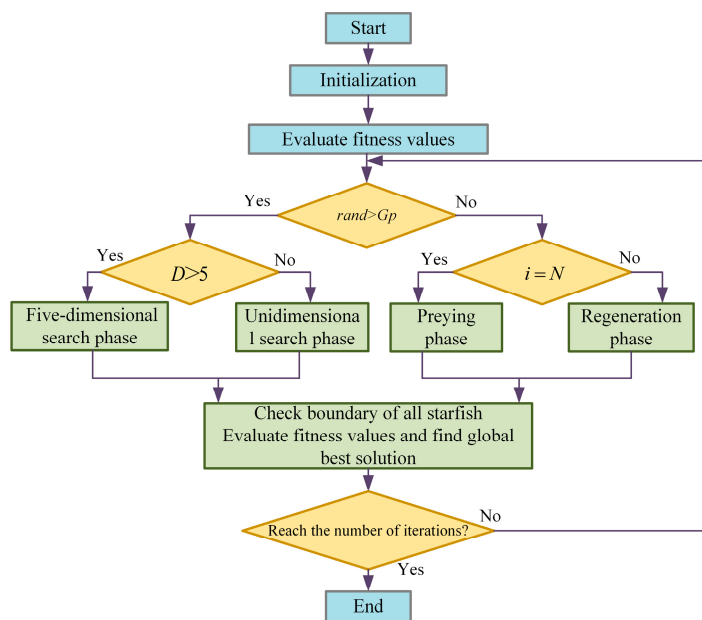


**Figure 3.** Flowchart of the SFOA.

By searching for the optimal parameter set, the SFOA minimizes the error between the terminal voltage that the model predicts and the actual terminal voltage.

### 2.3. REKF Based on a Fractional-Order Model

A state-space representation of the fractional-order equivalent circuit model must be established before applying the EKF for dynamic system estimation:

$$x_k = f(x_{k-1}, u_{k-1}) + \omega_{k-1} = Ax_{k-1} + Bu_{k-1} - \sum_{j=1}^k K_j x_{k-j} + \omega_{k-1} \quad (6)$$

$$y_k = h(x_k, u_k) + v_k = \mathbf{C}x_k - R_0u_k + U_{OCV} + v_k \quad (7)$$

where  $x_k$  is the state vector,  $y_k$  is the observation value,  $\omega_k$  is the process noise whose covariance matrix is  $Q_k$ , and  $v_k$  is the observation noise whose covariance matrix is  $R_k$ .

The EKF provides an optimal estimate in the minimum error sense only if both the process and measurement noise are Gaussian white noise with known statistical properties. If this condition is not satisfied, the EKF performance degrades. In contrast, the  $H\infty$  filter employs a minimax criterion, designed to minimize the worst-case estimation error caused by disturbances, thereby significantly improving robustness [35,36].

The robust Extended Kalman Filter based on the fractional-order (FOREKF) is formulated by integrating the robustness of the  $H\infty$  filter into the traditional EKF framework. Based on the fractional-order battery model from Equations (5) and (6), the cost function  $J$  is defined as follows:

$$J = \frac{\sum_{k=0}^N \|x_k - \hat{x}_k\|_{S_k}^2}{\|x_0 - \hat{x}_0\|_{P_0^{-1}}^2 + \sum_{k=0}^N \|w_k\|_{Q_k^{-1}}^2 + \sum_{k=0}^N \|v_k\|_{R_k^{-1}}^2} \quad (8)$$

where  $P_0$  is the covariance matrix of the initial error, and  $S_j$  is a positive definite matrix.

The  $H\infty$  filter is designed to minimize the upper bound of the cost function  $J$ :

$$\min_{\hat{x}_k} \max_{w_k, v_k, x_0} J < \gamma \quad (9)$$

As a key design parameter, the value of  $\gamma$  must be balanced against the need for minimum variance and optimal filtering performance.

The specific FOREKF procedure is as follows:

- (1) Initialize the parameters  $x_0, P_0, Q_0, R_0$ .
- (2) Calculate the predicted values of the state variable and prior estimation error covariance matrix:

$$\begin{cases} \hat{x}_k^- = A_{k-1}\hat{x}_{k-1}^+ + B_{k-1}u_{k-1} - \sum_{j=1}^L K_j \hat{x}_{k-j}^+ + \omega_{k-1} \\ P_k^- = (A_{k-1} - K_1)P_{k-1}^+ (A_{k-1} - K_1)^T + \sum_{j=2}^L K_j P_{k-j}^+ K_j^T + Q_{k-1} \end{cases} \quad (10)$$

- (3) Calculate the Kalman gain matrix and extended residual covariance matrix:

$$\begin{cases} K_k = P_k^- H_k^T (H_k P_k^- H_k^T + R_k)^{-1} \\ R_{e,k} = \begin{bmatrix} R_k & 0 \\ 0 & -\gamma I \end{bmatrix} + \begin{bmatrix} H_k \\ I \end{bmatrix} P_k^- \begin{bmatrix} H_k^T & I \end{bmatrix} \end{cases} \quad (11)$$

- (4) Update of state variables, observations, and estimation error covariance matrix:

$$\begin{cases} \hat{x}_k^+ = \hat{x}_k^- + K_k(y_k - \hat{y}_k) \\ \hat{y}_k = H_k \hat{x}_k - R_k u_k \\ P_k^+ = P_k^- - P_k^- \begin{bmatrix} H_k^T & I \end{bmatrix} R_{e,k}^{-1} \begin{bmatrix} H_k \\ I \end{bmatrix} \end{cases} \quad (12)$$

where  $I$  is the identity matrix. Steps (2) and (4) are repeated iteratively for each time step  $k = 1, 2, \dots$  until the sampling period concludes.

#### 2.4. SOE Estimation Based on FOASTFREKF

The FOREKF, while based on the EKF framework, is optimal only under the assumption of fixed noise statistics. However, this assumption is often invalid for real-world

battery systems, which exhibit time-varying noise properties, leading to reduced estimation accuracy. The REKF uses a first-order Taylor expansion to achieve local linearization in nonlinear systems. It retains only the Jacobian matrix but discards all higher-order terms. The iterative mechanism of the REKF means the current estimate depends heavily on the previous state estimate. When battery operating conditions change abruptly, this reliance can cause large estimation errors, which may accumulate over time and compromise performance or cause filter divergence.

To address these limitations and improve stability and accuracy, an adaptive mechanism is integrated into the FOREKF to enable real-time adjustment of noise statistics under dynamic operational conditions. Additionally, a time-varying attenuation factor  $\lambda_k$  is introduced to lessen the algorithm's dependence on historical data.

### (1) Adaptive updating of $Q_k$ and $R_k$ :

The adaptive noise estimation mechanism uses a sliding window approach to dynamically adjust the  $Q_k$  and  $R_k$  noise covariance matrices by monitoring the statistical characteristics of the new information sequence in real-time.

The new information  $d_k$  and the filtered residual information  $r_k$  are defined as follows:

$$\begin{cases} d_k = H_k(x_k - \hat{x}_k^-) + v_k \\ r_k = y_k - \hat{y}_k = R_k C_{d_k}^{-1} d_k \end{cases} \quad (13)$$

$$C_{d_k} = \begin{cases} \frac{k-1}{k} C_{d_{k-1}} + \frac{1}{k} d_k d_k^T & k \leq \omega \\ \frac{1}{\omega} \sum_{i=k-\omega+1}^k d_i d_i^T & k > \omega \end{cases} \quad (14)$$

where  $C_{d_k}$  is the covariance of the new interest rate estimate, and  $\omega$  is the length of the sliding data window. This paper uses a window length of 70.

Adaptive update noise is as follows:

$$\begin{cases} Q_{k-1} = K_k C_{d_k} K_k^T \\ R_k = C_{d_k} + H_k P_k H_k^T \end{cases} \quad (15)$$

### (2) Strong tracking state update:

A time-varying attenuation factor,  $\lambda_k$ , is introduced from the Strong Tracking Filter (STF) to modify the estimated error covariance matrix to enforce the orthogonality of the new state sequence. This technique strengthens the algorithm's tracking capability during abrupt state changes by assigning less weight to historical data. The modified prior estimation error covariance matrix update formula is as follows:

$$P_{k,\lambda}^- = \lambda_k \left[ (A_{k-1} - K_1) P_{k-1}^+ (A_{k-1} - K_1)^T + \sum_{j=2}^L K_j P_{k-j}^+ K_j^T \right] + Q_{k-1} \quad (16)$$

where the calculation formula of  $\lambda_k$  is as follows:

$$\lambda_k = \begin{cases} \lambda_0 & \lambda_0 \geq 1 \\ 1 & \lambda_0 < 1 \end{cases} \quad (17)$$

$$\lambda_0 = \frac{\text{tr}(V_k - H_k Q_{k-1} H_{k+1}^T - R_k)}{\text{tr}(A_k P_{k-1} A_k^T H_k^T H_k)} \quad (18)$$

$$V_k = \begin{cases} r_1 r_1^T & k=1 \\ \frac{\rho V_{k-1} + r_k r_k^T}{1+\rho} & k > 1 \end{cases} \quad (19)$$

where  $\rho$  is a forgetting factor, determined according to the specific model and application requirements.

## 2.5. Joint Estimation Method for SOE and SOH Across Multiple Time Scales

The SOE exhibits rapid changes during battery charging and discharging phases, whereas the SOH and related parameters are markedly more stable, often remaining consistent over one or more full charge–discharge cycles. Conventional single-timescale estimation methods struggle to accommodate these divergent dynamic characteristics, resulting in substantially increased computational complexity. To overcome this challenge, this paper proposes a multi-timescale joint estimation framework.

The discrete system equations for the multi-timescale joint estimation algorithm are as follows:

$$\begin{cases} x_k = f_x(x_{k-1}, \theta_{l-1}, u_{k-1}) + \omega_{k-1} \\ \theta_l = f_\theta(\theta_{l-1}) + \omega_{l-1} \\ z_k = g(x_k, \theta_l, u_k) + v_k \end{cases} \quad (20)$$

where  $x_k = [U_{1,k} \ U_{2,k} \ SOE_k]^T$ ,  $\theta_l = [R_0 \ R_1 \ R_2 \ CPE_1 \ CPE_2 \ mnQ_n]^T$ .

In the joint estimation framework,  $x_k$  is the state observer,  $\theta_l$  is the parameter observer, and  $Q_n$  is the maximum available capacity.  $\omega_{k-1}$ ,  $\omega_{l-1}$ , and  $v_k$  is the process noise.  $k$  is the time scale of the state observer, and  $l$  is the time scale of the parameter observer. To ensure the validity of the estimation results, this paper sets  $k$  to 1 s and  $l$  to 60 s.

The system state observer utilizes the FOASTFREKF algorithm to estimate the SOE. It operates on a fast timescale of seconds, enabling real-time tracking of current and voltage dynamics. The system parameter observer employs FOEKF to estimate SOH and update battery model parameters online. It operates on a slow timescale of minutes, tracking parameters that change slowly, such as capacity decay and internal resistance drift.

The specific process for estimating system parameters using FOEKF is as follows:

- (1) Initialize the parameters  $\theta_0$ ,  $P_0$ ,  $Q_0$ .
- (2) Calculation of the predicted values of the state variable and prior estimation error covariance matrix:

$$\begin{cases} \hat{\theta}_l^- = \hat{\theta}_{l-1}^+ \\ P_l^- = P_{l-1}^+ + Q_{l-1} \end{cases} \quad (21)$$

- (3) Calculation of the Kalman gain matrix:

$$K_l = P_l^- H_l^T (H_l P_l^- H_l^T + R_l)^{-1} \quad (22)$$

- (4) Update of state variables and estimation error covariance matrix:

$$\begin{cases} \hat{\theta}_l^+ = \hat{\theta}_l^- + K_l(z_k - \hat{z}_k) \\ P_l^+ = (I - K_l H_{l+1}) P_l^- \end{cases} \quad (23)$$

Once the first state observer has completed its estimation, its state variables will serve as input for the second parameter observer. At the same time, the parameter variable estimates from the second observer will be fed into the first observer. This bidirectional data exchange, combined with the multi-timescale framework, enables the joint estimation of SOE and SOH. The complete workflow is depicted in Figure 4.

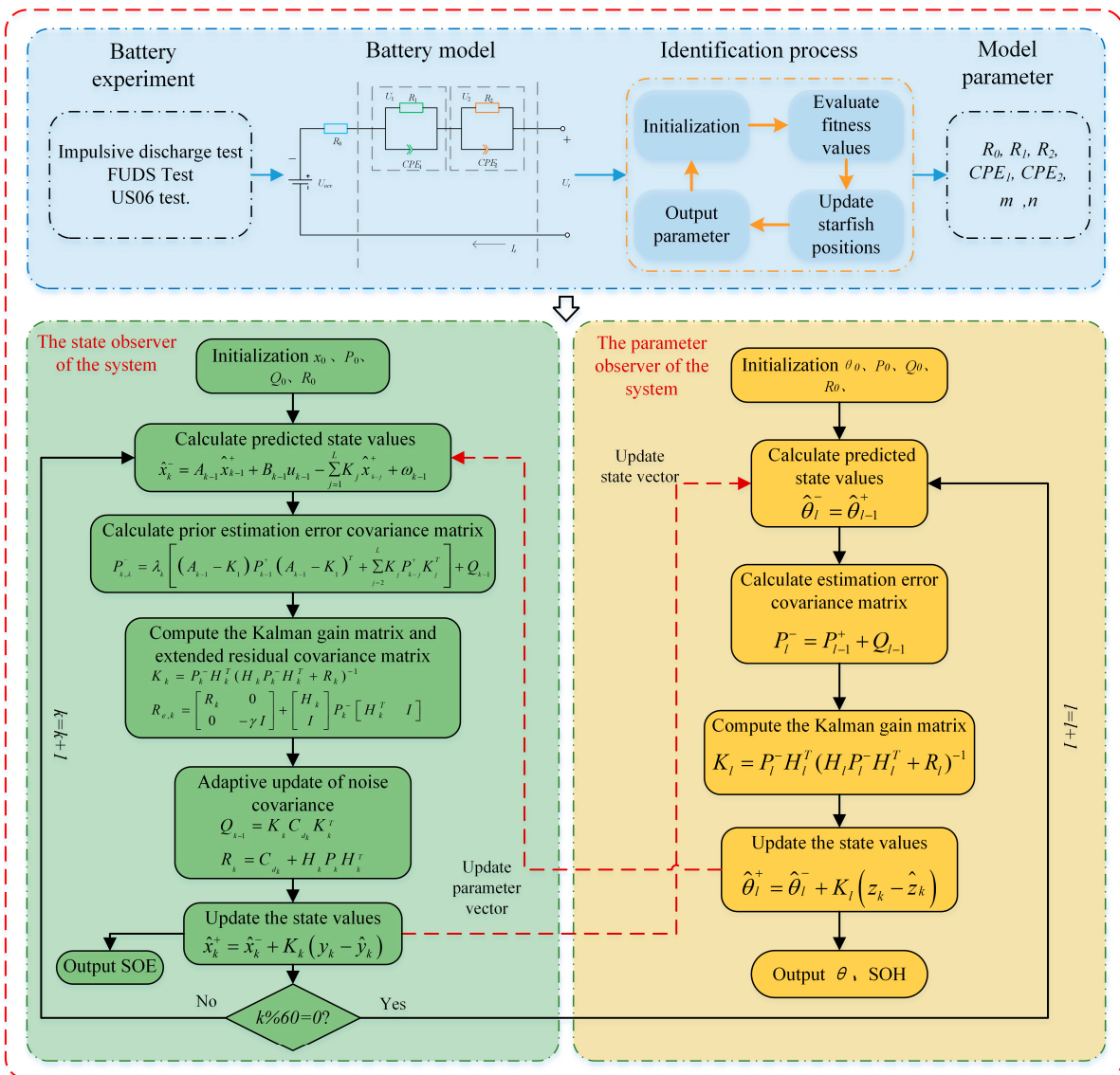


Figure 4. Flowchart of the joint estimation of SOE and SOH.

### 3. Results

#### 3.1. Battery Experiment

Figure 5 illustrates the configuration of the experimental testing platform for lithium-ion batteries. This platform consists of a constant temperature and humidity chamber, a BTS CT-4008T battery testing system (5 V/12 A) manufactured by Xinwei in Shenzhen, China, and a host computer. The 18650 NCM batteries used for testing are produced by Tianjin Lishen in Tianjin, China. Table 1 displays the battery's specification parameters.

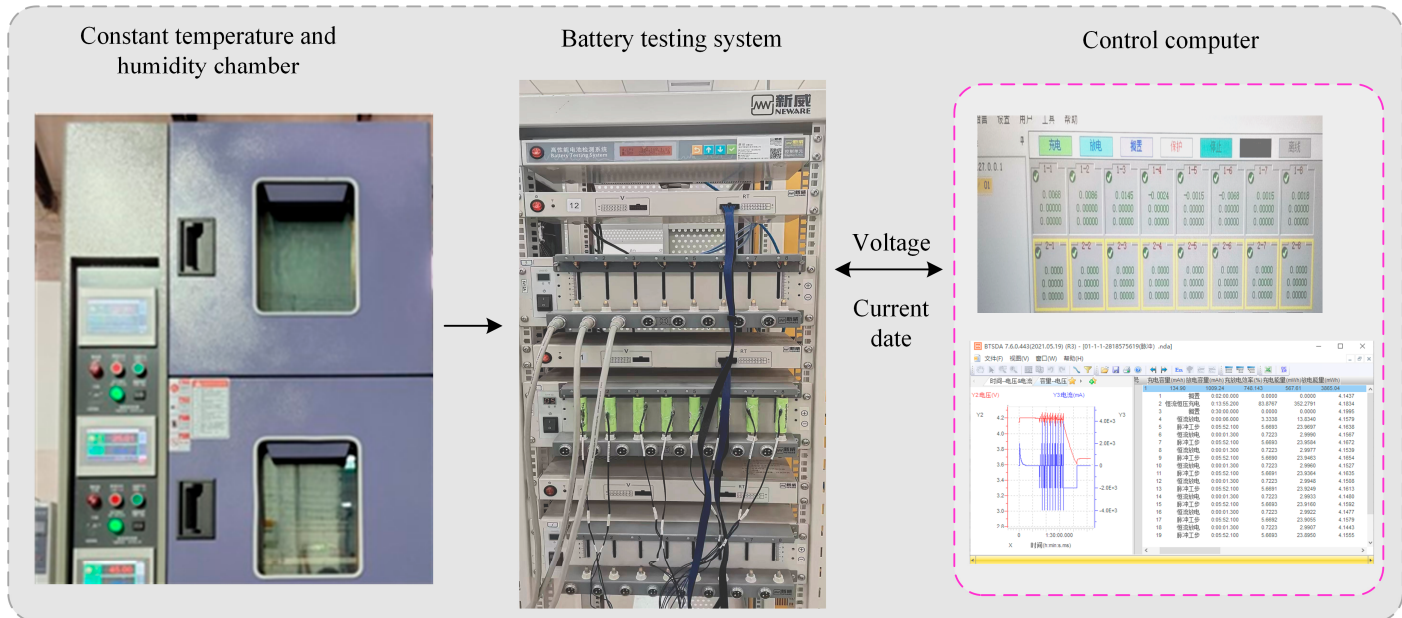
Table 1. Parameters of the batteries.

Parameter	Values
Rated capacity	2 Ah
rated voltage	3.6 V
Charge cutoff voltage	4.2 ± 0.05 V
Discharge cutoff voltage	2.5 V

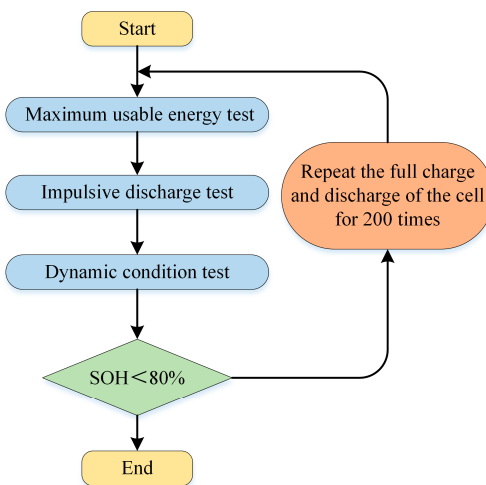
To confirm the proposed estimation method's efficacy in complex situations, this study designed and conducted battery aging experiments at typical ambient temperatures (25 °C).

Figure 6 illustrates the following experimental procedures:

- (1) To ascertain the battery's original capacity, the maximum useable energy test is performed.
- (2) The battery is subjected to charge–discharge cycling with a 1 C current. Each 200 cycles constitute one aging cycle.
- (3) Following each aging cycle, conduct the maximum usable capacity test, impulsive discharge test, and dynamic condition test (FUDS and US06).
- (4) Repeat steps 2 and 3 until the SOH status drops below 80%; at that point, the experiment is over.



**Figure 5.** Battery experimental testing platform.



**Figure 6.** Experimental flow chart.

### 3.2. Parameter Identification Results

This paper utilized three batteries at different aging conditions, corresponding to SOH values of 100%, 90.2%, and 83.03%. Using the impulsive discharge test data obtained in Section 3.1, the parameters  $R_0$ ,  $R_1$ ,  $R_2$ ,  $CPE_1$ ,  $CPE_2$ ,  $m$ , and  $n$  were identified using SFOA, with the results presented in Table 2. The identified parameters from both the SFOA and AGA methods were validated by comparing the simulated circuit model output to the

measured voltage. The verification results are shown in Figure 7. Model accuracy and estimation performance were quantified using mean error (ME), maximum error (Max Error), and root mean square error (RMSE). The terminal voltage estimation errors for battery models parameterized with SFOA and AGA are summarized in Table 3.

**Table 2.** Model parameters identified by the SFOA.

SOH	R0 ( $\Omega$ )	R1 ( $\Omega$ )	R2 ( $\Omega$ )	CPE1 (F)	CPE2 (F)	m	n
100%	0.0265	0.0228	0.0344	1143.59	42,142.86	0.9232	0.9864
90.20%	0.0334	0.0306	0.0399	1454.70	21,285.71	0.9727	0.9895
83.03%	0.0317	0.0344	0.0725	600	16,970.70	0.9690	0.9643

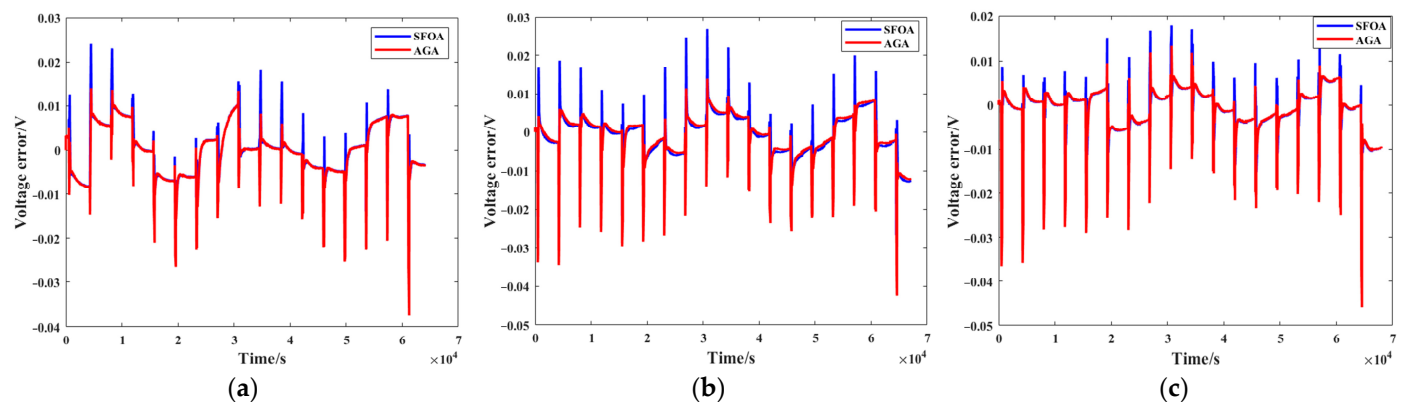


**Figure 7.** Voltage error comparison of different optimization algorithms: (a) Voltage error comparison at SOH = 100%; (b) Voltage error comparison at SOH = 90.20%; (c) Voltage error comparison at SOH = 83.03%.

**Table 3.** Terminal voltage estimation error.

SOH	Algorithms	ME (%)	Max Error (%)	RMSE
100%	SFOA	0.46	2.4	0.56
	AGA	0.48	3.75	0.63
90.20%	SFOA	0.42	2.92	0.55
	AGA	0.46	4.24	0.65
83.03%	SFOA	0.32	3.17	0.42
	AGA	0.37	4.58	0.59

The battery models parameterized with the SFOA demonstrated smaller voltage errors across all aging conditions than those identified with the AGA. This result confirms the SFOA's superior precision and robustness for parameter identification. Specifically, the SFOA-identified models achieved lower errors than the traditional AGA and maintained a consistent overall error below 0.032 V. This further confirms that SFOA enhances the accuracy of modeled systems.

### 3.3. Validation of the SOE Estimation Methods

#### 3.3.1. Analysis of SOE Estimation Results

This paper conducted tests under various driving conditions (FUDS and US06) and aging conditions (100%, 90.20%, and 83.03%). To test the algorithm's ability to adjust when faced with larger initial error values, the SOE initial value was set to 0.8, with the true value being 1. For comparative analysis, the EKF, FOEKF, FOREKF, FOSTFREKF, and FOASTFREKF were selected as comparison algorithms. Figures 8 and 9 present the SOE estimation results and error curves under various driving and aging situations, while Tables 4 and 5 summarize the quantitative error statistics.

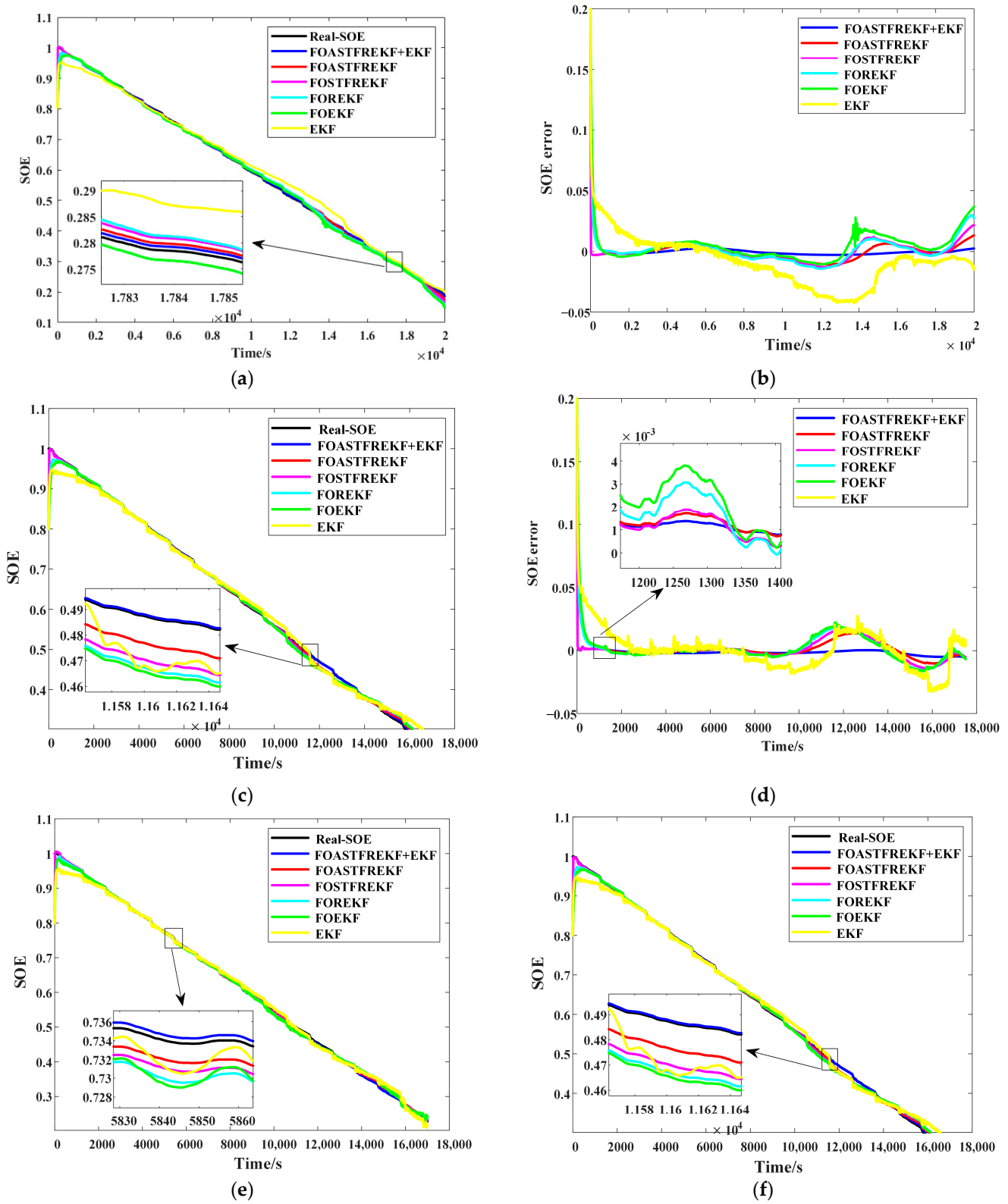


**Figure 8.** SOE estimation and error curves under FUDS condition: (a) SOE estimation curves at SOH = 100%; (b) error comparison curves at SOH = 100%; (c) SOE estimation curves at SOH = 90.20%; (d) error comparison curves at SOH = 90.20%; (e) SOE estimation curves at SOH = 83.03%; (f) error comparison curves at SOH = 83.03%.

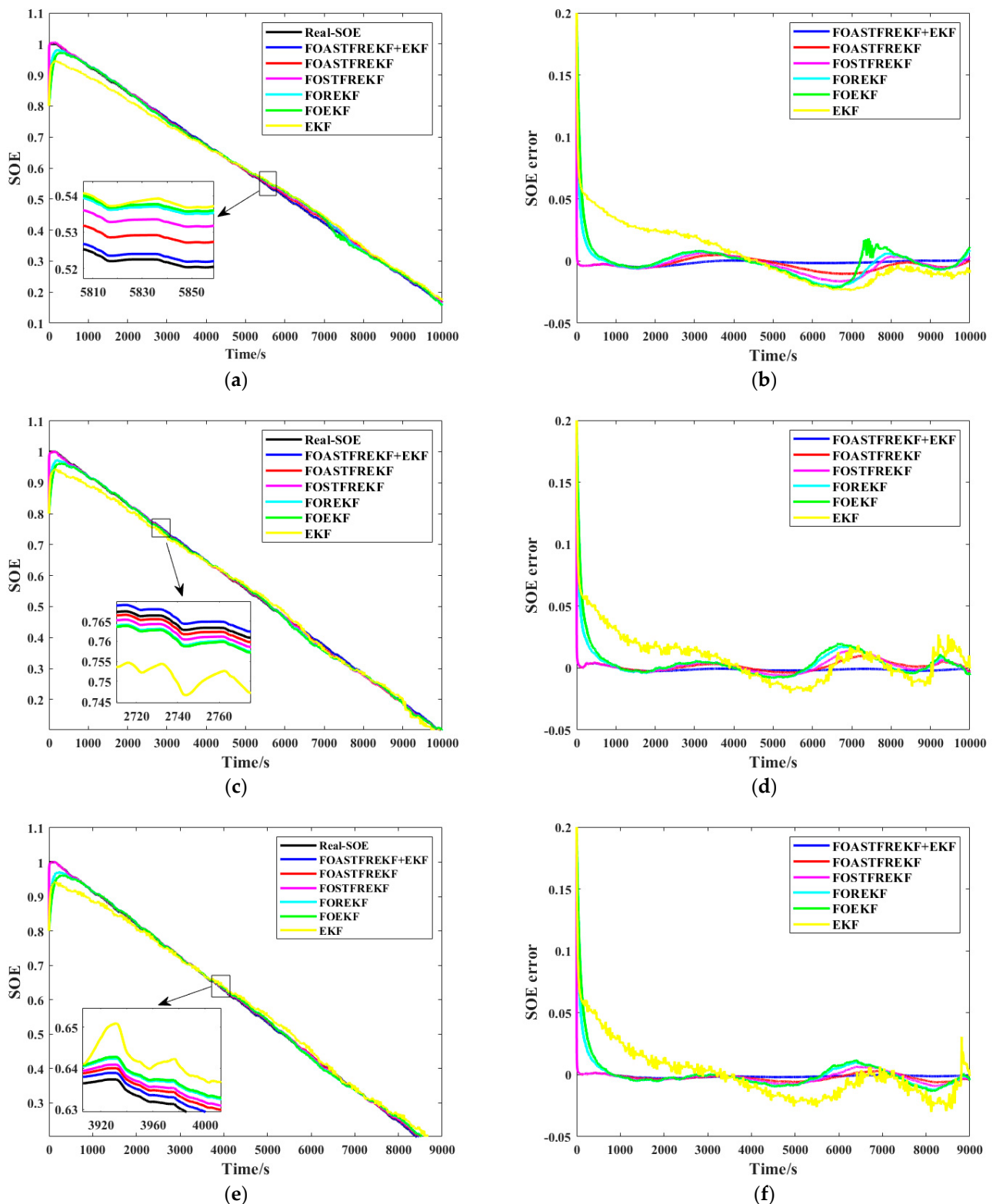


**Figure 9.** SOE estimation and error curves under US06 condition: (a) SOE estimation curves at SOH = 100%; (b) error comparison curves at SOH = 100%; (c) SOE estimation curves at SOH = 90.20%; (d) error comparison curves at SOH = 90.20%; (e) SOE estimation curves at SOH = 83.03%; (f) error comparison curves at SOH = 83.03%.

**Table 4.** SOE estimation error under FUDS condition.

SOH	Algorithms	ME (%)	Max Error (%)	RMSE
100%	EKF	1.5	4.29	1.94
	FOEKF	0.71	3.71	0.96
	FOREKF	0.60	2.99	0.81
	FOSTFREKF	0.55	2.16	0.69
	FOASTFREKF	0.44	1.33	0.53
	FOASTFREKF + EKF	0.15	0.29	0.18
90.20%	EKF	0.93	3.31	1.21
	FOEKF	0.58	2.53	0.82
	FOREKF	0.55	2.06	0.78
	FOSTFREKF	0.49	1.77	0.71
	FOASTFREKF	0.39	1.43	0.56
	FOASTFREKF + EKF	0.17	0.52	0.21
83.03%	EKF	0.68	2.8	0.88
	FOEKF	0.48	1.94	0.65
	FOREKF	0.45	1.55	0.62
	FOSTFREKF	0.42	1.22	0.55
	FOASTFREKF	0.35	0.93	0.45
	FOASTFREKF + EKF	0.18	0.50	0.21

**Table 5.** SOE estimation error under US06 condition.

SOH	Algorithms	ME (%)	Max Error (%)	RMSE
100%	EKF	1.48	3.36	1.69
	FOEKF	0.71	2.36	0.91
	FOREKF	0.65	2.04	0.85
	FOSTFREKF	0.56	1.63	0.71
	FOASTFREKF	0.44	1.02	0.51
	FOASTFREKF + EKF	0.15	0.48	0.21
90.20%	EKF	1.15	3.63	1.3
	FOEKF	0.58	3.24	0.79
	FOREKF	0.53	2.23	0.7
	FOSTFREKF	0.41	1.47	0.54
	FOASTFREKF	0.30	0.97	0.37
	FOASTFREKF + EKF	0.16	0.43	0.17
83.03%	EKF	1.14	3.06	1.37
	FOEKF	0.53	2.90	0.67
	FOREKF	0.50	1.87	0.60
	FOSTFREKF	0.38	0.90	0.45
	FOASTFREKF	0.29	0.61	0.34
	FOASTFREKF + EKF	0.14	0.29	0.16

The results demonstrate that SOE estimates converge rapidly to the true value under all tested operating conditions. Figures 8 and 9 indicate that the FOASTFREKF-EKF algorithm achieves the closest alignment with the reference curve. Furthermore, the FOEKF shows superior accuracy and stability over the EKF across different driving and aging conditions, confirming that the fractional-order model better captures the battery's nonlinear dynamics. In Figures 8 and 9b, the FOREKF displays significantly less volatility than the FOEKF, demonstrating that the integration of  $H_\infty$  filtering improves the algorithm's robustness. Figures 8 and 9b,d,f reveal that the FOASTFREKF and FOASTFREKF-EKF algorithms feature faster convergence and higher accuracy than the other three algorithms, a capability attributed to the inclusion of a time-varying attenuation factor and an adaptive strategy, which collectively enhance estimation performance.

As summarized in Tables 4 and 5, the FOASTFREKF-EKF algorithm achieves significantly higher SOE estimation accuracy than the other five benchmark algorithms across all tested driving and aging conditions. The joint estimation framework yields a substantial reduction in RMSE, ME, and maximum error for SOE compared to the standalone FOASTFREKF, with an overall error reduction exceeding 50%. This demonstrates that the proposed method preserves high accuracy under diverse operating scenarios. Specifically, the maximum error remains below 0.52%, the ME below 0.18%, and the RMSE below 0.21% in all cases. These results confirm that the proposed joint estimation algorithm enables precise SOE estimation under challenging operating and aging conditions.

To provide a comprehensive statistical comparison of the estimation performance across different algorithms, the box plots of the SOE estimation errors are presented in Figure 10. The analysis shows that the FOASTFREKF-EKF algorithm proposed in this paper has a significantly lower median error than the other five algorithms across all operating conditions, reflecting its superior estimation accuracy. Moreover, its corresponding box is shorter, indicating a smaller interquartile range (IQR), and its whiskers are considerably shorter. This demonstrates the method's highly stable estimation results, exhibiting minimal sensitivity to variations in battery operating conditions. The traditional EKF algorithm shows multiple outliers at the top of its box plot, suggesting a propensity for estimation divergence. In contrast, the proposed algorithm has few or no outliers, confirming its exceptional robustness.

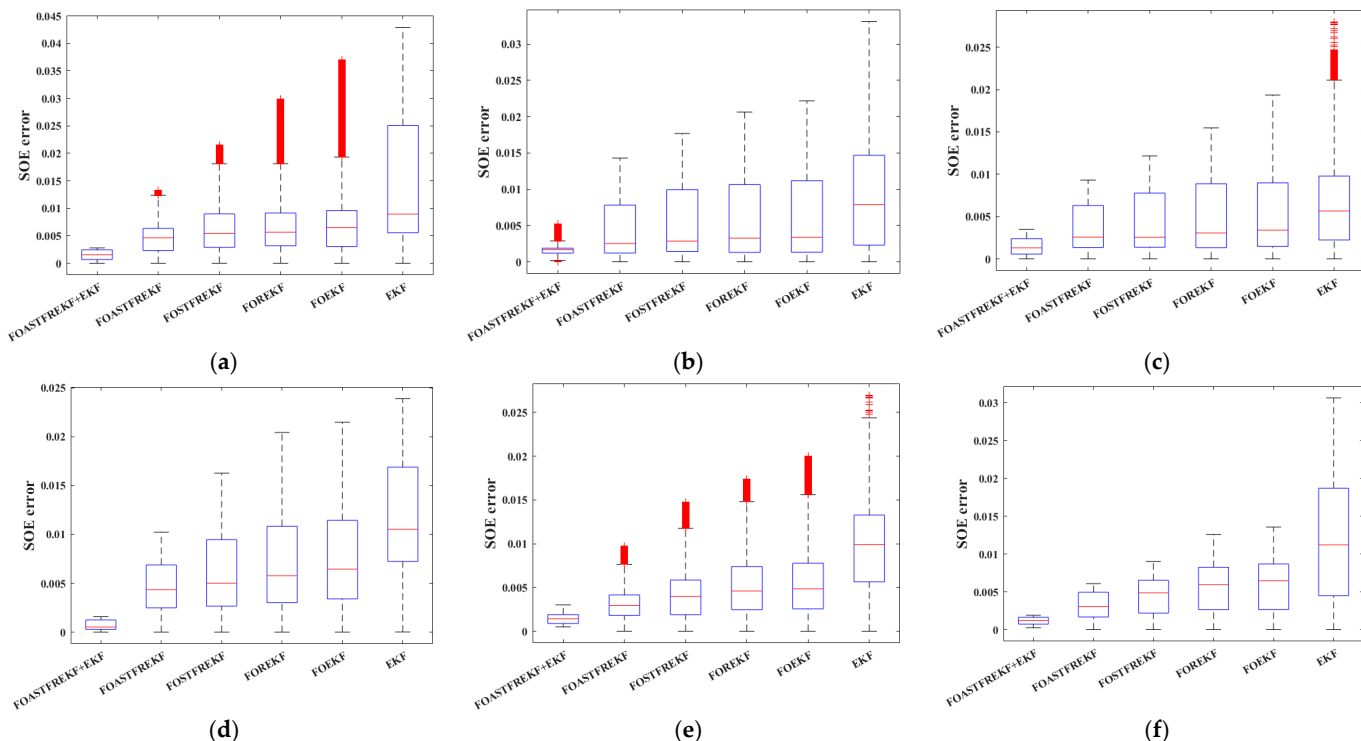


**Figure 10.** Box plots of SOE estimation errors for different algorithms: (a) SOE errors at SOH = 100% under FUDS condition; (b) SOE errors at SOH = 90.20% under FUDS condition; (c) SOE errors at SOH = 83.03% under FUDS condition; (d) SOE errors at SOH = 100% under US06 condition; (e) SOE errors at SOH = 90.20% under US06 condition; (f) SOE errors at SOH = 83.03% under US06 condition.

### 3.3.2. Performance Evaluation and Comparative Study

To evaluate the performance of the proposed algorithm, we compare it with other estimation methods from the literature. Based on a fractional-order model, Reference [37] utilizes a dual adaptive Unscented Kalman filter for the cooperative estimation of SOC and SOH, reporting excellent accuracy and robustness under various complex operating

conditions. Similarly, Reference [38] employs a first-order FOM with a square root cubature Kalman filter to estimate SOC and capacity, demonstrating its accuracy under varying battery states and temperatures. Tables 6 and 7 provide a detailed comparison, while error curves are illustrated in Figures 11 and 12.

**Table 6.** SOE estimation error with other methods under FUDS condition.

SOH	Algorithms	ME (%)	Max Error (%)	RMSE
100%	FOASTFREKF + EKF	0.15	0.29	0.18
	FOAUKF + AUKF	0.66	1.68	0.80
	FOSRCKF	0.72	3.72	0.82
90.20%	FOASTFREKF + EKF	0.17	0.52	0.21
	FOAUKF + AUKF	0.88	1.89	0.99
	FOSRCKF	0.46	1.81	0.64
83.03%	FOASTFREKF + EKF	0.18	0.50	0.21
	FOAUKF + AUKF	0.59	1.32	0.65
	FOSRCKF	1.31	2.99	1.52

**Table 7.** SOE estimation error with other methods under US06 condition.

SOH	Algorithms	ME (%)	Max Error (%)	RMSE
100%	FOASTFREKF + EKF	0.15	0.48	0.21
	FOAUKF + AUKF	0.99	1.49	1.04
	FOSRCKF	1.05	1.90	1.16
90.20%	FOASTFREKF + EKF	0.16	0.43	0.17
	FOAUKF + AUKF	1.00	1.75	1.12
	FOSRCKF	0.49	1.26	0.57
83.03%	FOASTFREKF + EKF	0.14	0.29	0.15
	FOAUKF + AUKF	0.45	0.82	0.50
	FOSRCKF	1.38	2.27	1.56

The results demonstrate that, under all test conditions, the FOASTFREKF-EKF algorithm rapidly converges to the reference value with minimal error. As illustrated in Figures 8 and 9, the proposed FOASTFREKF-EKF algorithm closely tracks the reference curve. Furthermore, data in Tables 4 and 5 confirm that the proposed algorithm achieved the smallest values for all three estimation error metrics across all tested driving and aging conditions. These findings collectively indicate a superior performance relative to other methods documented in the literature. This performance advantage arises from the comprehensive consideration of factors influencing estimation accuracy and the implementation of corresponding optimizations. Moreover, the refined identification method incorporates a more accurate battery model, which mitigates uncertainties introduced by experimental data errors.

### 3.4. Validation of the SOH Estimation Method

Figures 13 and 14 present a comparison between the estimated and measured SOH values. Table 8 summarizes the ME, max error, and RMSE after SOH estimation stabilization for each driving condition and aging condition. As shown in the figures, the algorithm exhibits minor fluctuations, but these are confined to a narrow range. Specifically, the maximum error remains below 0.57%, the ME below 0.23%, and the RMSE below 0.31% across both driving cycles. These results demonstrate that the multi-timescale joint estimation algorithm delivers accurate SOH estimates while simultaneously providing precise SOE determination under different aging conditions.

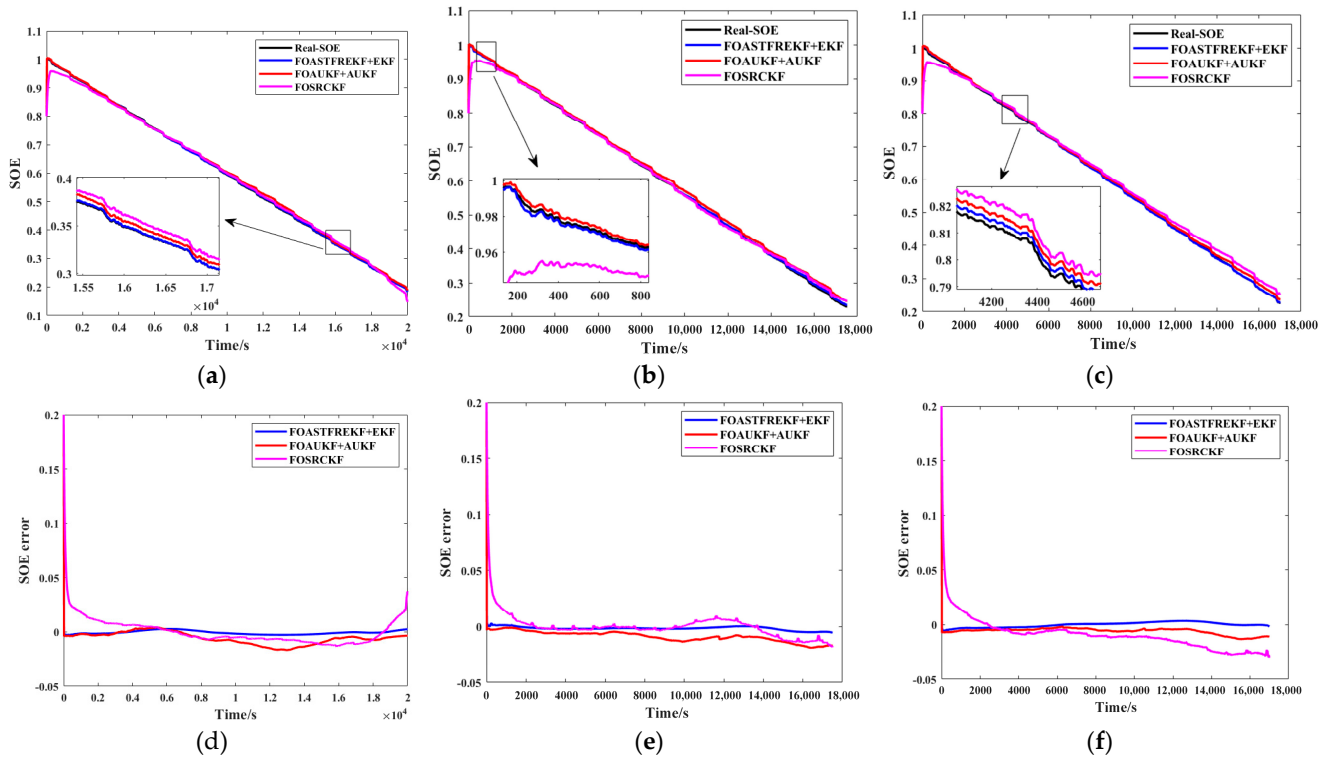


**Figure 11.** SOE estimation and error curves under FUDS condition: (a) SOE estimation curves at SOH = 100%; (b) SOE estimation curves at SOH = 90.20%; (c) SOE estimation curves at SOH = 83.03%; (d) error comparison curves at SOH = 100%; (e) error comparison curves at SOH = 90.20%; (f) error comparison curves at SOH = 83.03%.

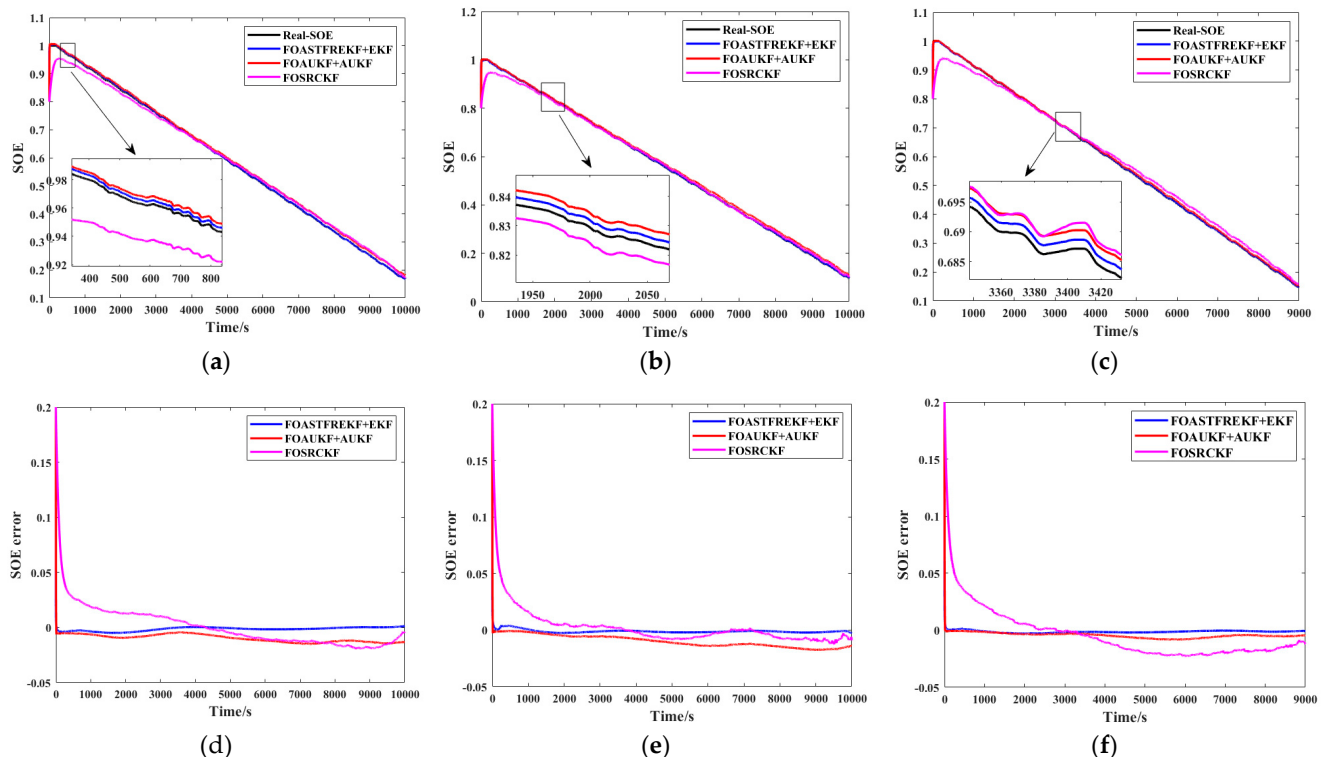


**Figure 12.** SOE estimation and error curves under US06 condition: (a) SOE estimation curves at SOH = 100%; (b) SOE estimation curves at SOH = 90.20%; (c) SOE estimation curves at SOH = 83.03%; (d) error comparison curves at SOH = 100%; (e) error comparison curves at SOH = 90.20%; (f) error comparison curves at SOH = 83.03%.

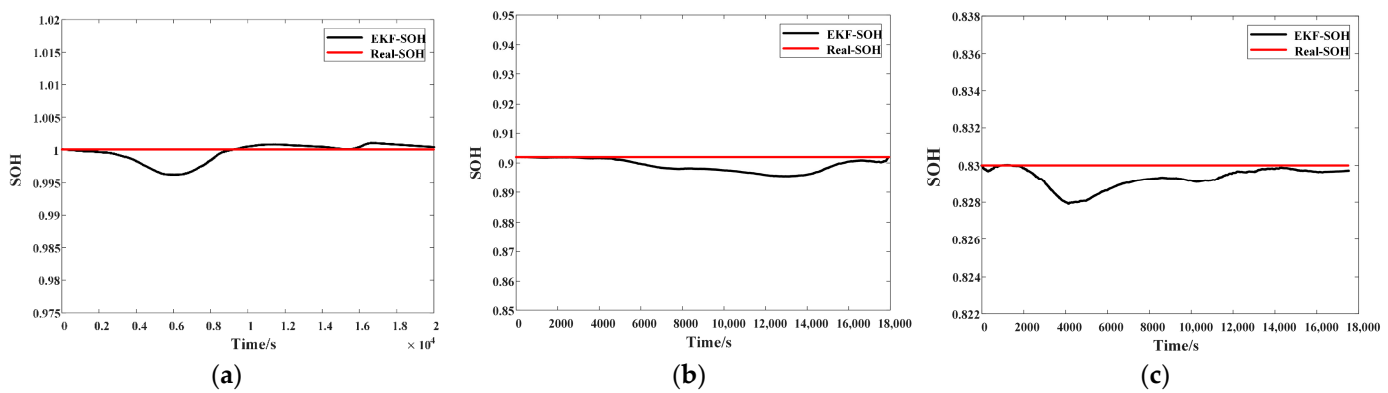


**Figure 13.** Comparison of SOH estimates and actual value under FUDS condition: (a) SOH = 100%; (b) SOH = 90.20%; (c) SOH = 83.03%.

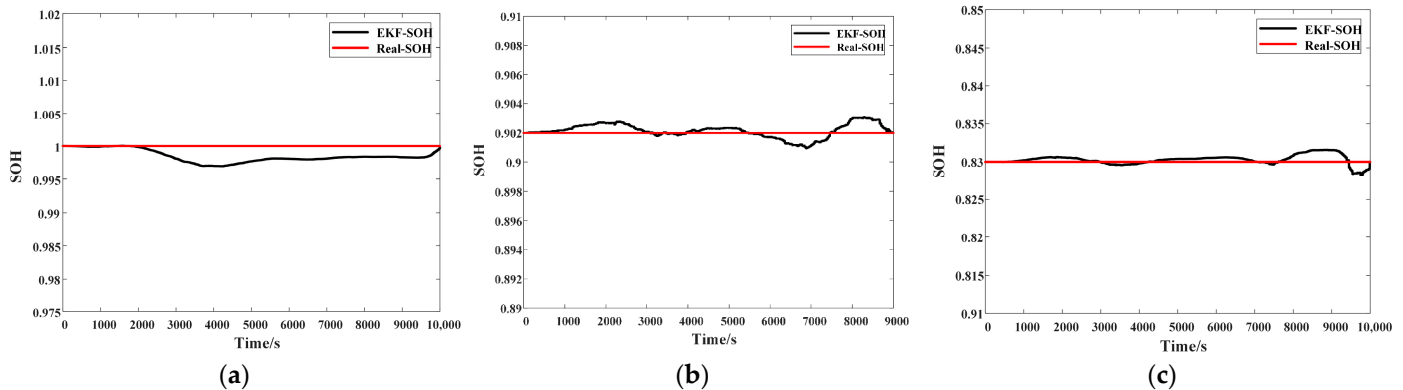


**Figure 14.** Comparison of SOH estimates and actual value under US06 condition: (a) SOH = 100%; (b) SOH = 90.20%; (c) SOH = 83.03%.

**Table 8.** Estimation error of SOH.

Conditions	SOH	ME (%)	Max Error (%)	RMSE
FUDS	100%	0.23	0.43	0.27
	90.20%	0.10	0.37	0.14
	83.03%	0.23	0.57	0.31
US06	100%	0.08	0.25	0.11
	90.20%	0.05	0.17	0.07
	83.03%	0.06	0.20	0.08

To quantitatively assess the overall accuracy, stability, and robustness of the SOH estimation method, we conducted a box plot analysis of the SOH estimation error across all tested driving and aging conditions, depicted in Figure 15.

The results show that the median maximum SOH error remained below 0.25% across all six test conditions, confirming that the proposed method provides estimates close to the reference values under most operating conditions. Furthermore, the narrow interquartile range (IQR) indicates that the vast majority of estimation errors are contained within a limited band, demonstrating low variability and high consistency. Moreover, the SOH error distribution contains few outliers, all of which lie close to the main data cluster. This finding suggests that the method effectively suppresses aberrant estimation errors, even under complex conditions such as rapid changes in dynamic characteristics or noise interference during aging.

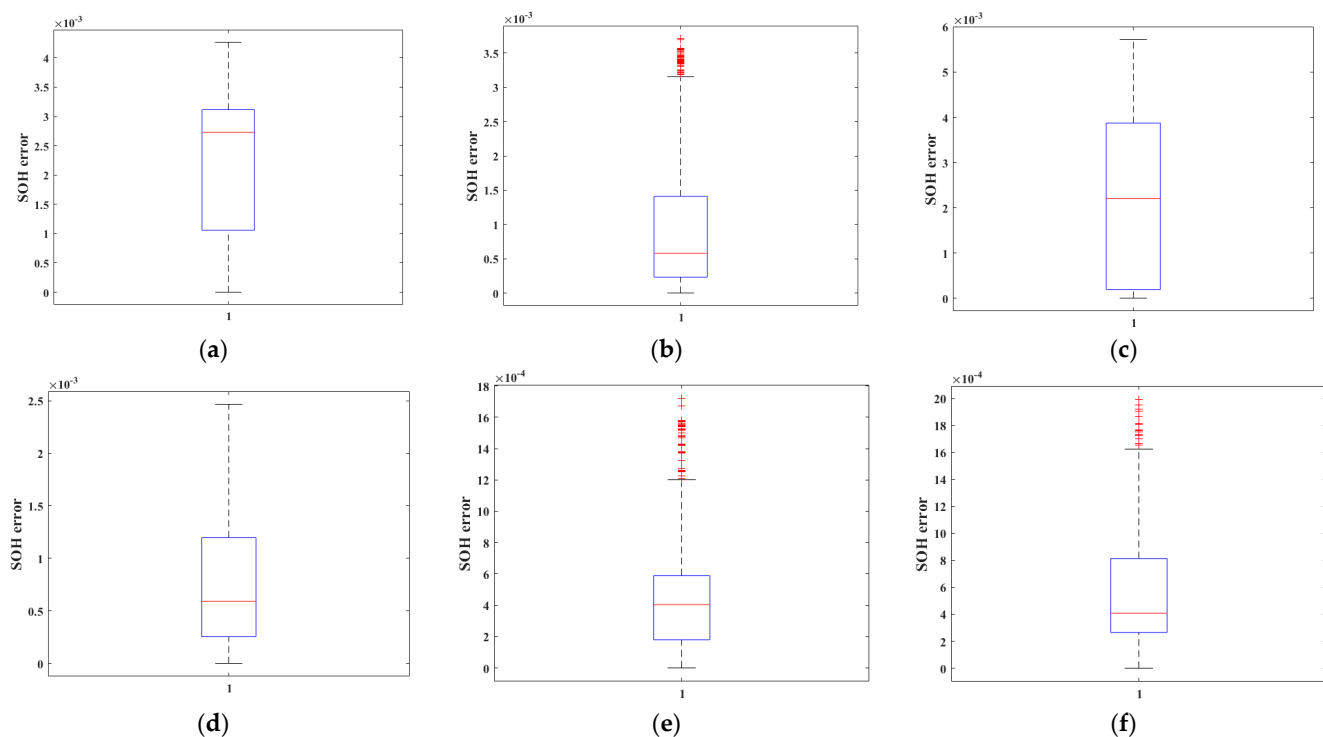


**Figure 15.** Box plots of SOH estimation errors for different algorithms: (a) SOH errors at SOH = 100% under FUDS condition; (b) SOH errors at SOH = 90.20% under FUDS condition; (c) SOH errors at SOH = 83.03% under FUDS condition; (d) SOH errors at SOH = 100% under US06 condition; (e) SOH errors at SOH = 90.20% under US06 condition; (f) SOH errors at SOH = 83.03% under US06 condition.

#### 4. Conclusions

To improve the accuracy and robustness of State of Energy (SOE) and State of Health (SOH) estimation while reducing computational complexity, this study proposes a joint estimation approach for lithium-ion batteries based on a fractional-order model. The proposed framework begins by establishing a fractional-order equivalent circuit model, whose parameters are identified offline using the Starfish Optimization Algorithm (SFOA) for enhanced model fidelity. Subsequently, an H<sub>oo</sub> filter is integrated into the structure to improve robustness against model uncertainties and external disturbances, forming the Fractional-Order Robust Extended Kalman Filter (FOREKF) framework. Furthermore, an adaptive noise covariance adjustment mechanism is incorporated to minimize the influence of operational noise. A time-varying attenuation factor is also included to enhance state tracking and response capabilities during sudden system changes, enabling accurate online SOE estimation.

This paper employs an Extended Kalman Filtering (EKF) for online battery parameter identification and SOH estimation, thereby accounting for the influence of parameter aging on SOE accuracy. Furthermore, a multi-timescale joint estimation algorithm for SOE and SOH is introduced, which effectively decouples the state coupling between the fast-varying SOE and the slow-varying SOH. This approach mitigates the impact of model errors on SOE estimation.

Experimental validation under diverse operating conditions demonstrates that the proposed algorithm achieves SOE estimation ME, Max error, and RMSE values consistently fall below 0.005. Similarly, for SOH estimation, the ME, Max error, and RMSE values remain below 0.0057. In comparison to other mainstream methods, the proposed algorithm provides superior accuracy and adaptability, offering a reliable solution for the joint battery state estimation under complex operating conditions.

**Author Contributions:** Conceptualization, F.Y. and J.Y.; methodology, F.Y. and J.Y.; software, J.Y.; validation, J.Y.; formal analysis, J.Y.; investigation, J.Y.; resources, F.Y.; data curation, J.Y.; writing—original draft preparation, J.Y.; writing—review and editing, F.Y.; visualization, J.Y.; supervision, F.Y.; project administration, F.Y.; funding acquisition, F.Y. All authors have read and agreed to the published version of the manuscript.

**Funding:** This research received no external funding.

**Data Availability Statement:** The data presented in this study are available on request from the corresponding author due to confidentiality agreements.

**Conflicts of Interest:** The authors declare no conflicts of interest.

## References

1. An, F.; Jiang, J.; Zhang, W.; Zhang, C.; Fan, X. State of Energy Estimation for Lithium-Ion Battery Pack via Prediction in Electric Vehicle Applications. *IEEE Trans. Veh. Technol.* **2022**, *71*, 184–195. [[CrossRef](#)]
2. Xiao, Y.; Song, W.; Liu, W.; Wan, F. Estimation of lithium battery state of charge using the LTG-SABO-GRU model. *Meas. Sci. Technol.* **2024**, *35*, 115106. [[CrossRef](#)]
3. Nyamathulla, S.; Dhananjayulu, C. A review of battery energy storage systems and advanced battery management system for different applications: Challenges and recommendations. *J. Energy Storage* **2024**, *86*, 111179. [[CrossRef](#)]
4. Wei, M.; Ye, M.; Li, J.B.; Wang, Q.; Xu, X. State of Charge Estimation of Lithium-Ion Batteries Using LSTM and NARX Neural Networks. *IEEE Access* **2020**, *8*, 189236–189245. [[CrossRef](#)]
5. Laadjal, K.; Marques Cardoso, A.J. A review of supercapacitors modeling, SoH, and SoE estimation methods: Issues and challenges. *Int. J. Energy Res.* **2021**, *45*, 18424–18440. [[CrossRef](#)]
6. Wang, Y.; Tian, J.; Sun, Z.; Wang, L.; Xu, R.; Li, M.; Chen, Z. A comprehensive review of battery modeling and state estimation approaches for advanced battery management systems. *Renew. Sustain. Energy Rev.* **2020**, *131*, 110015. [[CrossRef](#)]
7. Shrivastava, P.; Soon, T.K.; Bin Idris, M.Y.I.; Mekhilef, S.; Adnan, S.B.R.S. Combined state of charge and state of energy estimation of lithium-ion battery using dual forgetting factor-based adaptive extended Kalman filter for electric vehicle applications. *IEEE Trans. Veh. Technol.* **2021**, *70*, 1200–1215. [[CrossRef](#)]
8. Shrivastava, P.; Naidu, P.A.; Sharma, S.; Panigrahi, B.K.; Garg, A. Review on technological advancement of lithium-ion battery states estimation methods for electric vehicle applications. *J. Energy Storage* **2023**, *64*, 107159. [[CrossRef](#)]
9. Zhang, X.; Wang, Y.; Wu, J.; Chen, Z. A novel method for lithium-ion battery state of energy and state of power estimation based on multi-time-scale filter. *Appl. Energy* **2018**, *216*, 442–451. [[CrossRef](#)]
10. Zhang, J.; Xiao, B.; Niu, G.; Xie, X.; Wu, S. Joint estimation of state-of-charge and state-of-power for hybrid supercapacitors using fractional-order adaptive unscented Kalman filter. *Energy* **2024**, *294*, 130942. [[CrossRef](#)]
11. Zhang, X.G.; Duan, L.C.; Gang, Q.S.; Wang, Y.; Song, H. State of charge estimation for lithium-Ion battery based on adaptive extended Kalman filter with improved residual covariance matrix estimator. *J. Power Sources* **2024**, *589*, 233758. [[CrossRef](#)]
12. Dong, G.; Chen, Z.; Wei, J.; Zhang, C.; Wang, P. An online model-based method for state of energy estimation of lithium-ion batteries using dual filters. *J. Power Sources* **2016**, *301*, 277–286. [[CrossRef](#)]
13. Lai, X.; Qin, C.; Gao, W.; Zheng, Y.; Yi, W. A state of charge estimator based extended Kalman filter using an electrochemistry-based equivalent circuit model for lithium-ion batteries. *Appl. Sci.* **2018**, *8*, 1592. [[CrossRef](#)]
14. He, Z.G.; Fu, X.R.; Pan, C.F.; Zhang, X.; Ji, X.; Hu, S. Research on lithium battery state of charge estimation based on improved Adaptive Iterative eXogenous Kalman Filter and multidimensional estimation scheme. *J. Energy Storage* **2024**, *97*, 112763. [[CrossRef](#)]
15. Mawonou, K.S.R.; Eddahech, A.; Dumur, D.; Beauvois, D.; Godoy, E. Improved state of charge estimation for li-ion batteries using fractional order extended Kalman filter. *J. Power Sources* **2019**, *435*, 226710. [[CrossRef](#)]
16. Sockeel, N.; Ball, J.; Shahverdi, M.; Mazzola, M. Passive tracking of the electrochemical impedance of a hybrid electric vehicle battery and state of charge estimation through an extended and unscented Kalman filter. *Batteries* **2018**, *4*, 52. [[CrossRef](#)]
17. Yang, F.H.; Zhang, S.H.; Li, W.H.; Miao, Q. State-of-charge estimation of lithium-ion batteries using LSTM and UKF. *Energy* **2020**, *201*, 117664. [[CrossRef](#)]
18. Peng, J.K.; Luo, J.Y.; He, H.W.; Lu, B. An improved state of charge estimation method based on cubature Kalman filter for lithium-ion batteries. *Appl. Energy* **2019**, *253*, 113520. [[CrossRef](#)]
19. Mercorelli, P. A Hysteresis Hybrid Extended Kalman Filter as an Observer for Sensorless Valve Control in Camless Internal Combustion Engines. *IEEE Trans. Ind. Appl.* **2012**, *48*, 1940–1949. [[CrossRef](#)]
20. Liu, C.Z.; Liu, W.Q.; Wang, L.Y.; Hu, G.; Ma, L.; Ren, B. A new method of modeling and state of charge estimation of the battery. *J. Power Sources* **2016**, *320*, 1–12. [[CrossRef](#)]

21. Guo, R.; Shen, W. Lithium-ion battery state of charge and state of power estimation based on a partial-adaptive fractional-order model in electric vehicles. *IEEE Trans. Ind. Electron.* **2023**, *70*, 10123–10133. [[CrossRef](#)]
22. He, L.; Wang, Y.Y.; Wei, Y.J.; Wang, M.; Hu, X.; Shi, Q. An adaptive central difference Kalman filter approach for state of charge estimation by fractional order model of lithium-ion battery. *Energy* **2022**, *244*, 122627. [[CrossRef](#)]
23. Guo, D.; Yang, G.; Feng, X.; Han, X.; Lu, L.; Ouyang, M. Physics-based fractional-order model with simplified solid phase diffusion of lithium-ion battery. *J. Energy Storage* **2020**, *30*, 101404. [[CrossRef](#)]
24. Tang, X.; Wang, Y.; Yao, K.; He, Z.; Gao, F. Model migration based battery power capability evaluation considering uncertainties of temperature and aging. *J. Power Sources* **2019**, *440*, 227141. [[CrossRef](#)]
25. Chen, L.; Wang, S.; Jiang, H.; Fernandez, C. A novel combined estimation method for state of energy and predicted maximum available energy based on fractional order modeling. *J. Energy Storage* **2023**, *62*, 106930. [[CrossRef](#)]
26. Wei, Z.; Zhao, J.; Ji, D.; Tseng, K.J. A multi-timescale estimator for battery state of charge and capacity dual estimation based on an online identified model. *Appl. Energy* **2017**, *204*, 1264–1274. [[CrossRef](#)]
27. Lai, X.; Weng, J.; Huang, Y.; Yuan, M.; Yao, Y.; Han, X.; Zheng, Y. A joint state-of-health and state-of-energy estimation method for lithium-ion batteries through combining the forgetting factor recursive least squares and unscented Kalman filter. *Measurement* **2022**, *205*, 112187. [[CrossRef](#)]
28. Long, T.; Wang, S.; Cao, W.; Zhou, H.; Fernandez, C. An improved variable forgetting factor recursive least square-double extend Kalman filtering based on global mean particle swarm optimization algorithm for collaborative state of energy and state of health estimation of lithium-ion batteries. *Electrochim. Acta* **2023**, *450*, 142270. [[CrossRef](#)]
29. Bello, I.T.; Raza, H.; Michael, A.T.; Muneeswara, M.; Tewari, N.; Bingsen, W.; Cheung, Y.N.; Choi, Z.; Boles, S.T. Charging Ahead: The Evolution and Reliability of Nickel-Zinc Battery Solutions. *EcoMat* **2025**, *7*, e12505. [[CrossRef](#)]
30. Wang, C.; Wang, X.; Yang, M.J.; Li, J.; Qian, F.; Zhang, Z.; Zhou, M.; Guo, X.; Wang, K. Concurrent estimation of lithium-ion battery charge and energy states by fractional-order model and multi-innovation adaptive cubature Kalman filter. *Energy* **2025**, *322*, 135498. [[CrossRef](#)]
31. Li, J.; Zhou, J.; Wu, X.; Liu, T. Wide temperature multi-condition SOC estimation for Li-ion batteries based on F-FOMIAEKF. *Meas. Sci. Technol.* **2025**, *36*, 025012. [[CrossRef](#)]
32. Chen, L.; Yu, W.; Cheng, G.; Wang, J. State-of-charge estimation of lithium-ion batteries based on fractional-order modeling and adaptive square-root cubature Kalman filter. *Energy* **2023**, *271*, 127007. [[CrossRef](#)]
33. Wu, J.; Fang, C.; Jin, Z.; Zhang, L.; Xing, J. A multi-scale fractional-order dual unscented Kalman filter based parameter and state of charge joint estimation method of lithium-ion battery. *J. Energy Storage* **2022**, *50*, 104666. [[CrossRef](#)]
34. Zhong, C.; Li, G.; Meng, Z.; Li, H.; Yildiz, A.R.; Mirjalili, S. Starfish optimization algorithm (SFOA): A bio-inspired metaheuristic algorithm for global optimization compared with 100 optimizers. *Neural Comput. Appl.* **2025**, *37*, 3641–3683. [[CrossRef](#)]
35. Zhuang, Y.; Wang, Z.; Yu, H.; Wang, W.; Lauria, S. A robust extended  $H_\infty$  filtering approach to multi-robot cooperative localization in dynamic indoor environments. *Control. Eng. Prac.* **2013**, *21*, 953–961. [[CrossRef](#)]
36. Chandra, K.P.B.; Gub, D.W.; Postlethwaite, I. A cubature  $H_\infty$  filter and its square-root version. *Int. J. Control.* **2014**, *87*, 764–776. [[CrossRef](#)]
37. Feng, F.; Teng, S.; Liu, K.; Xie, J.; Xie, Y.; Liu, B.; Li, K. Co-estimation of lithium-ion battery state of charge and state of temperature based on a hybrid electrochemical-thermal-neural-network model. *J. Power Sources* **2020**, *455*, 227935. [[CrossRef](#)]
38. Zeng, Y.; Li, Y.; Zhou, Z.; Zhao, D.; Yang, T.; Ren, P.; Zhang, C. Joint estimation of state of charge and health utilizing fractional-order square-root cubature Kalman filtering with order scheduling strategy. *Energy* **2025**, *320*, 135022. [[CrossRef](#)]

**Disclaimer/Publisher’s Note:** The statements, opinions and data contained in all publications are solely those of the individual author(s) and contributor(s) and not of MDPI and/or the editor(s). MDPI and/or the editor(s) disclaim responsibility for any injury to people or property resulting from any ideas, methods, instructions or products referred to in the content.